

# In-situ assembled cobalt-free PSFNru nanocomposites as bi-functional electrodes for direct ammonia symmetric solid oxide fuel cells

Zhixian Liang<sup>1</sup>, Shanshan Jiang<sup>1</sup>  , Zihao Xie<sup>1</sup>, Yongning Yi<sup>2</sup>, Jingjing Jiang<sup>3</sup>  , Wei Wang<sup>2</sup>, Huangang Shi<sup>4</sup>, Lei Ge<sup>5</sup>, and Chao Su<sup>1</sup>  

<sup>1</sup>School of Energy and Power, Jiangsu University of Science and Technology, Zhenjiang 212100, China

<sup>2</sup>State Key Laboratory of Materials-Oriented Chemical Engineering, College of Chemical Engineering, Nanjing Tech University, Nanjing 211816, China

<sup>3</sup>Institute of Analysis and Testing, Beijing Academy of Science and Technology, Beijing 100089, China

<sup>4</sup>International Joint Laboratory of Green & Low Carbon Development, School of Environmental Engineering, Nanjing Institute of Technology, Nanjing 211167, China

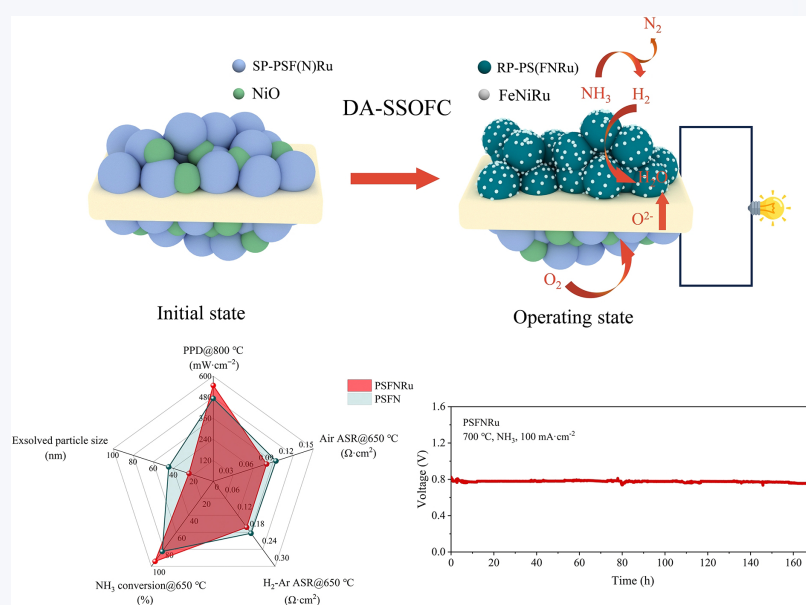
<sup>5</sup>Centre for Future Materials, School of Engineering, University of Southern Queensland, Springfield, QLD 4300, Australia

 Cite this article: *Nano Research*, 2025, 18, 94907402. <https://doi.org/10.26599/NR.2025.94907402>

**ABSTRACT:** Symmetric solid oxide fuel cells (SSOFCs) have gained significant attention owing to their cost-effective fabrication, superior thermomechanical compatibility, and enhanced long-term stability. Ammonia (NH<sub>3</sub>), an excellent hydrogen carrier, is a promising clean energy source with high energy density, easy transportation and storage. Notably, NH<sub>3</sub> contained only nitrogen and hydrogen, making it carbon-free. In this study, we synthesize the highly active symmetric electrode material Pr<sub>0.32</sub>Sr<sub>0.48</sub>Fe<sub>0.75</sub>Ni<sub>0.2</sub>Ru<sub>0.05</sub>O<sub>3-δ</sub> (PSFNru) by replacing partial Fe in Pr<sub>0.32</sub>Sr<sub>0.48</sub>Fe<sub>0.8</sub>Ni<sub>0.2</sub>O<sub>3-δ</sub> (PSFN) with 5 mol% Ru. PSFNru possesses a sufficient quantity of oxygen vacancies, with the capacity to *in-situ* exsolved alloy nanoparticles (ANPs) in a reducing atmosphere. This nanocomposite is found

to promote electrochemical reactions. For example, at 800 °C, the SSOFC employing the PSFNru electrode achieves a peak power density (PPD) of 736 mW·cm<sup>-2</sup> when using hydrogen (H<sub>2</sub>) as the fuel. Under NH<sub>3</sub> conditions, the cell delivers a PPD of 547 mW·cm<sup>-2</sup>, significantly surpassing the 462 mW·cm<sup>-2</sup> recorded for a comparable cell employing the PSFN electrode. The enhanced cell performance is mainly ascribed to Ru doping, which boosts the ORR activity and facilitates the *in-situ* exsolution of ANPs at the anode, increasing active sites and accelerating NH<sub>3</sub> decomposition. In addition, remarkable operational stability of the single cell (172 h under NH<sub>3</sub> fuel at 700 °C) is also demonstrated. These encouraging experimental results highlight the superiority of PSFNru as the bi-functional electrodes for direct ammonia symmetric solid oxide fuel cells (DA-SSOFCs), and providing a potential and reliable pathway towards accelerating the development of DA-SSOFCs.

**KEYWORDS:** symmetric solid oxide fuel cells (SSOFCs), ammonia fuel, nanocomposites, alloy nanoparticles exsolution



Received: March 13, 2025; Revised: March 22, 2025; Accepted: March 24, 2025

 Address correspondence to Shanshan Jiang, [jss522@just.edu.cn](mailto:jss522@just.edu.cn); Jingjing Jiang, [jiangjingjingnju@163.com](mailto:jiangjingjingnju@163.com); Chao Su, [chao.su@just.edu.cn](mailto:chao.su@just.edu.cn)

## 1 Introduction

Over the previous several years, the depletion of fossil fuels and the rise in greenhouse gas emissions have intensified the global focus on sustainable and clean energy alternatives [1–5]. Among these, fuel cells have been recognized as highly efficient conversion systems, capable of directly converting chemical fuels into electricity while reducing environmental impact to a minimum [6–10]. Enhancing the extended durability while ensuring the economic viability of solid oxide fuel cells (SOFCs) remains a crucial challenge in their advancement [11–14]. Recent research has demonstrated that certain oxides possess the capability to function as cathode and anode materials simultaneously, enabling the development of symmetric solid oxide fuel cells (SSOFCs). This not only reduces the fabrication costs, but also improves the operational stability because of thermomechanical compatibility between the electrolyte and the electrode. Therefore, SSOFCs have received much attention in recent years [15–17].

Hydrogen ( $H_2$ ) is widely recognized as a prospective energy source with broad research perspectives [18].  $H_2$  can be produced through the reforming of natural gas or coal, as well as from water cracking reactions powered by regenerative energy technologies (e.g., solar, wind, and tidal) [19–21]. It is also a commonly used fuel for SOFCs. Unfortunately, the commercialization of hydrogen energy is severely hindered by its insufficient bulk density and low liquefaction temperature, which results in high storage and transportation costs [22, 23]. A viable alternative that offers high energy density, renewable characteristics, and ease of storage is still being sought. Considering these considerations, hydrocarbon fuels, including methanol, ethanol, methane and ethane, have garnered growing interest in the past several years owing to their superior energy density and convenient storage. However, the carbon deposition caused by the high-temperature decomposition of these fuels has significantly hindered their use in SOFCs [24]. In contrast, ammonia offers notable benefits, including higher volumetric energy density, facile storage and transport, and well-established production technology. These benefits make the commercialization of direct ammonia solid oxide fuel cells (DA-SOFCs) possible [25–27].

For optimal performance in DA-SOFCs, the anode should exhibit high catalytic efficiency for both the hydrogen oxidation reaction (HOR) and the ammonia decomposition reaction (NDR) [28–30]. Although conventional nickel-based anodes display good HOR activity, their NDR catalytic activity is significantly reduced due to severe particle agglomeration at low temperatures [31]. Consequently, the innovation of efficient and durable anodes is crucial for DA-SOFCs. Perovskite-type oxides are extensively recognized as excellent cathode materials due to their structural stability and compositional flexibility. The superior catalytic activity of a perovskite oxide toward the oxygen reduction reaction (ORR), HOR and NDR facilitates the integration of SSOFCs technology with ammonia fuel, thereby promoting the development of DA-SOFCs. Among them,  $SrFeO_{3-\delta}$ -based perovskites demonstrate outstanding ORR catalytic capability, which is primarily attributed to their high concentration of oxygen vacancies and strong oxygen exchange capability [32, 33]. Furthermore, Zhou and his colleagues demonstrated that Ru doping in  $(La_{0.8}Sr_{0.2})_{0.9}Sc_{0.2}Mn_{0.8}O_{3-\delta}$  further increased the oxygen vacancy concentration in the cathode material, facilitating oxygen ion diffusion and exhibiting excellent ORR catalytic activity [34]. Nevertheless, pure perovskites materials used as anodes exhibit limited catalytic performance in facilitating

both HOR and NDR. To address this limitation, integrating transition metal elements into perovskite materials, along with employing an *in-situ* exsolution approach to generate nanoparticles (NPs), have been shown to significantly enhance HOR and NDR catalytic activity and durability [35]. This enhancement is ascribed to the embedded structure formed between the *in-situ* exsolved nanoparticles (NPs) and the perovskite matrix, which effectively suppresses the aggregation of the nanoparticles and thereby improves structural stability [36, 37]. Up to date, several studies have demonstrated that using bimetallic or alloy catalysts, such as Ru-Fe, Co-Fe, Fe-Ni and Ni-Ru, significantly improves the HOR and NDR catalytic efficiency while also enhancing their durability over extended periods [38–42]. However, for perovskites with a stoichiometric ratio of  $A/B = 1$  ( $ABO_3$ ), the exsolution of a significant number of alloy nanoparticles (ANPs) was a slow and prolonged process. Recently, introducing A-site deficiencies (i.e.,  $A/B < 1$ ) to enhance the driving force for B-site element exsolution emerged as a promising strategy. This approach facilitates the exsolution of a greater number of ANPs within a shorter timeframe [36]. For instance, Song et al. developed an A-site-deficient perovskite-type anode material of  $La_{0.52}Sr_{0.30}TiO_{3-\delta}$  (LST), which was decorated with Ni-Co ANPs on the anode surface through the *in-situ* exsolution method to achieve excellent electrochemical performance and operational stability. At 800 °C, using  $NH_3$  as fuel, the peak power density (PPD) of the single cell reached  $361 \text{ mW}\cdot\text{cm}^{-2}$  [43]. Qin et al. synthesized an advanced A-site-deficient anode material,  $(Pr_{0.5}Sr_{0.5})_{0.9}Fe_{0.9}Ru_{0.1}O_{3-\delta}$  based on  $SrFeO_{3-\delta}$ . Upon  $H_2$  treatment, *in-situ* exsolved FeRu alloy nanoparticles were uniformly distributed on the electrode surface, exhibiting excellent electronic/ionic conductivity and catalytic activity [36]. Therefore, the formation of ANPs with uniform dispersion across the anode surface represents an effective strategy for enhancing both HOR and NDR. This approach is crucial for the development of high-performance DA-SOFCs.

In this study, perovskite oxide  $Pr_{0.32}Sr_{0.48}Fe_{0.8}Ni_{0.2}O_{3-\delta}$  (PSFN) was selected as the parent material, and Ru ion were doped to develop a novel nanocomposite symmetric electrode material,  $Pr_{0.32}Sr_{0.48}Fe_{0.75}Ni_{0.2}Ru_{0.05}O_{3-\delta}$  (PSFNRu) for DA-SOFCs. The Ru doping effectively increased the oxygen vacancy concentration, accelerated oxygen ion migration, and enhanced ORR activity. Under reduction conditions, *in-situ* exsolved ANPs enlarged the specific surface area of the electrode, providing additional active sites for the anodic electrochemical reactions. Consequently, PSFNRu with 5 mol% Ru doping exhibited excellent catalytic performance for ORR, HOR and NDR. The single cell based on  $Sm_{0.2}Ce_{0.8}O_{1.9}$  (SDC) electrolyte achieved PPDs of 736 and  $547 \text{ mW}\cdot\text{cm}^{-2}$  at 800 °C when fueled with  $H_2$ ,  $NH_3$ , respectively. Furthermore, no significant performance degradation over 172 h at 700 °C using  $NH_3$  as fuel. This study offered profound insights into the rational design of symmetric electrode materials with enhanced activity and durability, offering a promising strategy for improving the performance and prolonged stability of DA-SOFCs, thereby facilitating their practical deployment.

## 2 Experimental

### 2.1 Powder preparation

The  $Pr_{0.32}Sr_{0.48}Fe_{0.8}Ni_{0.2}O_{3-\delta}$  (PSFN) and  $Pr_{0.32}Sr_{0.48}Fe_{0.75}Ni_{0.2}Ru_{0.05}O_{3-\delta}$  (PSFNRu) materials were prepared using the sol-gel method. Taking the synthesis of PSFNRu perovskite as an example,

the following brief description was provided.  $\text{PrN}_3\text{O}_9 \cdot 6\text{H}_2\text{O}$ ,  $\text{Ni}_2\text{O}_6\text{Sr}$ ,  $\text{Ni}(\text{NO}_3)_2 \cdot 6\text{H}_2\text{O}$ ,  $\text{FeN}_3\text{O}_9 \cdot 6\text{H}_2\text{O}$ , and  $\text{RuCl}_3$  metal nitrates (all analytical purity, Aladdin Chemical Reagent Co., Ltd.) were chosen as the cation sources. Based on the desired nominal composition of PSFNru perovskite, the metal nitrates were dissolved in water following stoichiometric ratios. Then, an appropriate amount of ethylenediaminetetraacetic acid (EDTA), citric acid (CA) complexing agents and ammonium hydroxide were added to the solution in a molar ratio of EDTA:CA:total metal ions of 1:2:1, aiming to achieve uniform mixing of the metal cations at the atomic level. After the removal of water by evaporation, a transparent gel was obtained, which was pre-decomposed under air at 250 °C. The synthesized precursors were subsequently calcined in air at 1100 °C for 5 h. The synthesized PSFN and PSFNru powders were subjected to a 10 vol.%  $\text{H}_2$ -Ar gas at 800 °C for 10 h, leading to reduced PSFN (r-PSFN) and PSFNru (r-PSFNru) samples, respectively.

## 2.2 Fabrication of cells

The  $\text{Sm}_{0.2}\text{Ce}_{0.8}\text{O}_{1.9}$  (SDC) electrolyte pellets were prepared via dry pressing, followed by sintering in air at 1400 °C for 5 h. The sintered dense electrolyte pellets were polished with sandpaper to achieve a thickness of 300  $\mu\text{m}$ . Subsequently, they were ultrasonically cleaned for 10 min to remove any surface impurities. The ground PSFN and PSFNru powders were mixed thoroughly with isopropanol, ethylene glycol, and glycerol to form cathode (anode) slurries through ball milling. Electrodes with an effective area of 0.47  $\text{cm}^2$  were spray-coated on both sides of the electrolyte and then sintered in air at 1100 °C for 2 h. Silver paste was applied for current collection during the fuel cell testing process, and silver wires were used for electron conduction.

## 2.3 Characterization

The crystal structure of the prepared electrode powders was characterized using X-ray diffraction (XRD, Bruker AXS D8 Advance) equipped with  $\text{Cu-K}\alpha$  radiation, with a scanning range of  $10^\circ \leq 2\theta \leq 90^\circ$  at increments of  $0.02^\circ$ . The valence state changes were analyzed by X-ray photoelectron spectroscopy (XPS, Thermofisher nexsa). Temperature-programmed tests were performed with a chemisorption analyzer (Builder, PCA-1200) equipped with a thermal conductivity detector (TCD). Catalytic activity tests for NDR were evaluated using various powders in a quartz tube reactor, with the effluent gases assessed through a gas chromatograph (GC-9860). Electrochemical impedance spectroscopy (EIS) of half cells under an air atmosphere was obtained using a Princeton impedance spectroscopy analyzer (PARSTAT MC 1000). EIS measurements in 10 vol.%  $\text{H}_2$ -Ar atmosphere were performed using a Solartron 1260 frequency response analyzer and a Solartron 1287 potentiostat. EIS under open circuit voltage conditions was obtained using an electrochemical workstation (DH-7002A). The distribution of relaxation times (DRT) technique was employed to analyze the EIS data. This approach enables the assessment of impedance variations over a range of frequencies using a specialized application designed by Ciucci et al [44]. The  $I$ - $V$ - $P$  data for the single cells were collected using a Keithley 2460 source meter. During the single-cell experiments, hydrogen or ammonia was delivered to the anode side at a fixed flow rate of 60  $\text{mL}\cdot\text{min}^{-2}$ , while the cathode was continuously in contact with ambient air. The conductivity of PSFNru and PSFN in air and 10 vol.%  $\text{H}_2$ -Ar atmosphere was

measured by the four-probe DC method using the Keithley 2460 source meter. Dense rods for conductivity measurements were obtained by sintering PSFNru and PSFN samples at 1200 °C. The surface morphology of the cells was employing scanning electron microscope (SEM, Zeiss 55VP) and a high-resolution transmission electron microscope (HR-TEM, G2T20). The composition of the samples was analyzed by energy-dispersive X-ray spectroscopy (EDX, G2 F30 STWIN).

## 3 Results and discussion

XRD analysis was conducted on the PSFN and PSFNru samples before and after exposure to a 10 vol.%  $\text{H}_2$ -Ar reducing atmosphere (Figs. S1(a)–S1(c) in the Electronic Supplementary Material (ESM)). As shown in Fig. S1(a) in the ESM, both PSFN and PSFNru powders primarily exhibited an orthorhombic crystal structure with a  $Pnma$  space group, accompanied by a minor formation of NiO (space group:  $Fm\bar{3}m$ ). It was observed that after doping with 5 mol% Ru into PSFN, no additional Ru-containing compounds were detected, indicating successful incorporation of Ru into the lattice. The enlarged view revealed that the main peak of the PSFNru sample shifted toward lower angle relative to the PSFN sample. This shift was ascribed to the larger ionic radius of Ru ions relative to Fe ions, ( $\text{Ru}^{3+}$ : 0.082 nm,  $\text{Fe}^{4+}$ : 0.059 nm,  $\text{Fe}^{3+}$ : 0.065 nm,  $\text{Fe}^{2+}$ : 0.078 nm) which affected the crystal lattice structure [16, 45]. In Fig. S1(c) in the ESM, it was observed that after treatment at 800 °C in a 10 vol.%  $\text{H}_2$ -Ar gas mixture, the original structure of PSFNru transformed into a Ruddlesden–Popper (RP) perovskite structure, with an  $I4/mmm$  space group, denoted as RP-PS(FNRu) [36], and was accompanied by the *in-situ* exsolution of a metallic alloy phase, FeNiRu. To further investigate the phase composition of the PSFN and PSFNru samples before and after reduction, the detailed analysis of the XRD patterns were conducted (Figs. 1(a) and 1(b), and Figs. S1(d) and S1(e) in the ESM). The fitting result for PSFN, with relatively low reliability factors ( $R_{\text{wp}} = 4.93\%$ ,  $R_p = 3.87\%$ ,  $\chi^2 = 1.12$ ), confirmed that the characteristic diffraction peaks of this material corresponded to NiO and a single perovskite phase, denoted as SP-PSF(N). From the fitting result of PSFNru, it could be observed that Ru doping does not introduce additional impurity phases. The diffraction peaks originate from NiO and a single perovskite phase, denoted as SP-PSF(N)Ru. Compared to PSFN, the phase composition remains essentially unchanged, which was in consistent with the previous analysis. Upon reduction, r-PSFNru exhibited the presence of two distinct phases, quantified as 89.1 wt.% of RP-PS(FNRu) and 10.9 wt.% of FeNiRu. In comparison to r-PSFN (9.5 wt.%), a greater amount of ANPs was present in r-PSFNru.

To better investigate the *in-situ* exsolution of ANPs, SEM testing was employed. SEM characterization revealed the presence of NiO particles on the surfaces of both PSFN and PSFNru samples (Figs. S2(a) and S2(b) in the ESM). The reduced samples, as depicted in Figs. S2(c) and S2(d) in the ESM, exhibited a higher density of particles on its surface, which was attributed to the *in-situ* exsolution of ANPs from the substrate induced by the reducing gas, consistent with the XRD results. Furthermore, a notably higher quantity of ANPs was observed on the r-PSFNru surface compared to r-PSFN. Statistical analysis based on Figs. S3(a) and S3(b) in the ESM indicated that the average particle size of the ANPs in r-PSFNru ( $\sim 25$  nm) was smaller than that in r-PSFN ( $\sim 45$  nm), suggesting that Ru doping effectively inhibited nanoparticle growth.

To further investigated the composition and elemental

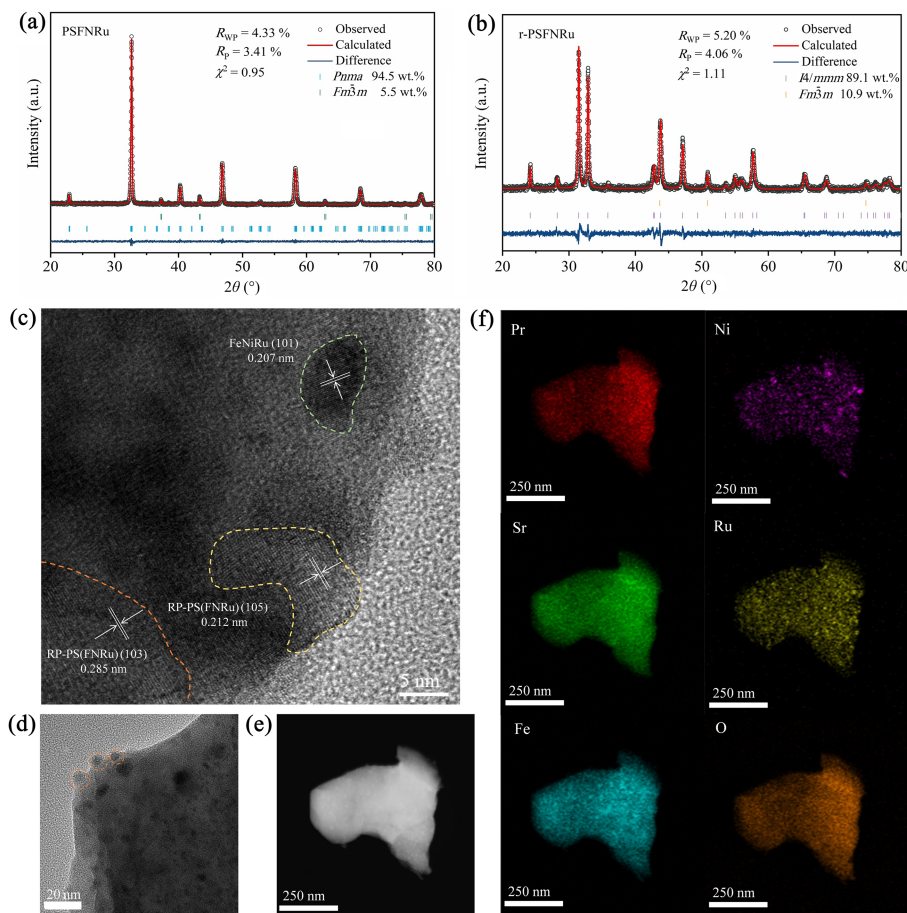


**Figure 1** XRD Rietveld refinement data of (a) PSFNru and (b) r-PSFNru. (c) HR-TEM, (d) TEM, (e) STEM images, and (f) EDX mapping of r-PSFNru.

distribution of the ANPs in the r-PSFNru sample, TEM was conducted. Additionally, HR-TEM analysis confirmed the presence of two different phases in r-PSFNru, as previously inferred from the XRD results. As illustrated in Fig. 1(c), two lattice spacings associated with RP-PS(FNRu) had been identified, along with a lattice spacing corresponding to the FeNiRu phase. The measured lattice spacings were approximately 0.285, 0.212 and 0.207 nm, which correspond to the (103), (105) and (101) diffraction planes of the respective crystalline structures. As shown in Fig. 1(d), some ANPs formed an embedded structure with the perovskite substrate during the *in-situ* exsolution process, exhibiting excellent anti-aggregation capability. The scanning transmission electron microscopy (STEM) image in Fig. 1(e) further shown a distribution of ANPs on the surface of the r-PSFNru sample. The elemental mapping obtained from EDX in Fig. 1(f) confirmed that these ANPs are FeNiRu alloy.

To demonstrate the feasibility of PSFNru as a symmetrical electrode, XPS was carried out to analyze the valence state changes of surface elements in PSFN and PSFNru before and after reduction. As observed in Fig. 2(a), the reduced samples exhibited the coexistence of Fe<sup>2+</sup>, Fe<sup>3+</sup>, Fe<sup>4+</sup> and Fe<sup>0</sup> oxidation states. The characteristic binding energies corresponding to these states were located at 723.1/709.76, 724.69/711.33, 726.89/713.92 and 720.08/706.70 eV, respectively. This indicated that after reduction, Fe ions were successfully exsolved from the perovskite lattice [25, 46]. Similarly, the Ni 2p spectra (Fig. 2(c)) revealed Ni<sup>2+</sup> (854.7 eV) and Ni<sup>3+</sup> (856.2 eV), with an additional Ni<sup>0</sup> peak (852.47 eV) appearing

after reduction [47, 48]. In Fig. 2(e), the Ru 3p spectra clearly showed that the valence states of Ru ions in the PSFNru sample were primarily Ru<sup>3+</sup> and Ru<sup>6+</sup>, with peaks at 464.2 and 466 eV, respectively. After reduction, a distinct Ru<sup>0</sup> (461.56 eV) signal was detected in the Ru 3p spectra [49]. Additionally, the Ru<sup>0</sup> peak at 279.41 eV was clearly observed in the Ru 3d spectra, as shown in Fig. S4 in the ESM. These results confirmed the successful *in-situ* exsolution of FeNi or FeNiRu ANPs from r-PSFN and r-PSFNru. Moreover, the higher content of Fe<sup>0</sup> in r-PSFNru compared to r-PSFN demonstrated that Ru doping facilitated the exsolution of FeNiRu ANPs, leading to the formation of a greater number of ANPs.

For the unreduced samples, as demonstrated in Figs. 2(b) and 2(d), the binding energies corresponding to their oxidation states exhibited no significant deviation from those observed in the reduced samples. However, a noticeable decrease in the valence state of B-site elements was observed upon Ru doping. This phenomenon was likely due to the partial substitution of Fe ions by high-valence Ru, which necessitated a spontaneous reduction in the oxidation state of B-site elements to maintain charge neutrality. This adjustment mitigated excessive lattice distortion that might arise from an elevated concentration of oxygen vacancies, thereby stabilizing the perovskite structure. The O 1s spectra of PSFN and PSFNru were presented in Fig. 2(f). The O 1s XPS results revealed that the binding energies for lattice oxygen (O<sup>2-</sup>), high oxidation state oxygen (O<sub>2</sub><sup>2-/O</sup>-), adsorbed oxygen (OH/O<sub>2</sub>), and H<sub>2</sub>O in PSFNru and PSFN were 528.35, 529.05, 531.20, and 532.80 eV,

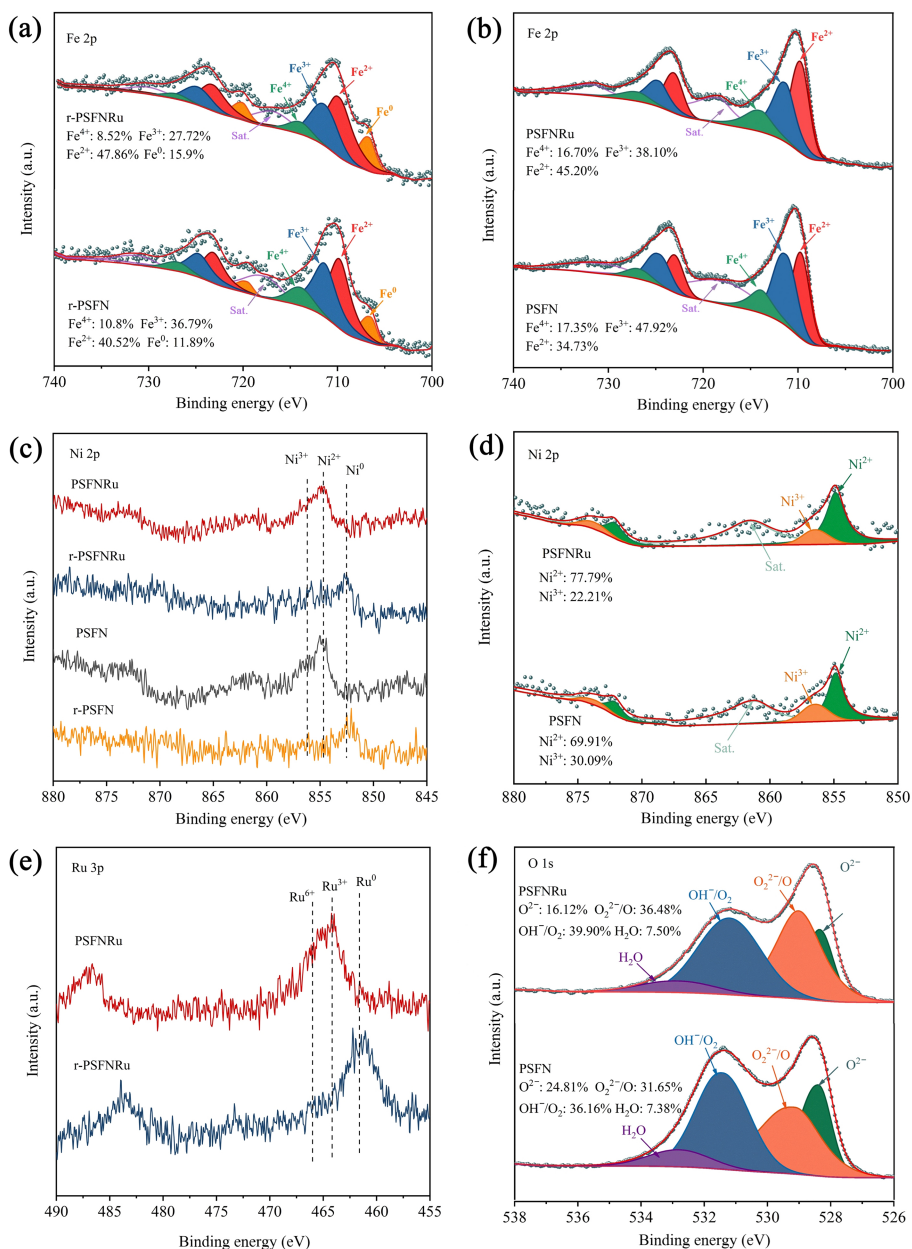


**Figure 2** Fe 2p XPS fitting of (a) r-PSFNrRu and r-PSFN, and (b) PSFNrRu and PSFN. Ni 2p XPS fitting of (c) PSFN, PSFNrRu, r-PSFN and r-PSFNrRu. Ni 2p XPS fitting of (d) PSFNrRu and PSFN. Ru 3p XPS of (e) PSFNrRu and r-PSFNrRu. O 1s XPS fitting of (f) PSFNrRu and PSFN.

respectively [50]. From the fitting results, it could be observed that, compared to PSFN, PSFNrRu exhibited a noticeable reduction in  $O^{2-}$  content, while the signal intensity of  $O_2^{2-}/O$  increased. Both phenomena suggested a higher concentration of oxygen vacancies in PSFNrRu. This could be due to Ru doping, which induced the reduction of Fe and Ni ions from higher to lower valence states, thereby lowering their average valence state and facilitating the formation of bulk oxygen vacancies, the additional oxygen vacancies could promote oxygen ion conduction and facilitated oxygen surface exchange [51, 52]. According to the literature, the content of  $O_2^{2-}/O$  is directly related to the oxygen activation capability of the catalyst [53]. This further confirmed the rationality of PSFNrRu as a symmetrical electrode.

Figure 3(a) shown the results of  $H_2$  temperature-programmed reduction ( $H_2$ -TPR) for PSFN and PSFNrRu samples. It could be

observed that PSFN exhibited five  $H_2$  consumption peaks at approximately 361 ( $T_1'$ ), 440 ( $T_2'$ ), 555 ( $T_3'$ ), 681 ( $T_4'$ ) and 861 °C ( $T_5'$ ), respectively, corresponding to the reduction of  $Fe^{4+/3+}$  to  $Fe^{2+}$ ,  $Ni^{3+}$  to  $Ni^{2+}$ ,  $Ni^{2+}$  to  $Ni^0$ ,  $Fe^{2+}$  to  $Fe^0$ , and the reduction of low-valent Fe and Ni ions to FeNi alloy [43, 54]. On the other hand, PSFNrRu displayed six  $H_2$  consumption peaks at approximately 251 ( $T_0$ ), 287 ( $T_1$ ), 410 ( $T_2$ ), 553 ( $T_3$ ), 673 ( $T_4$ ) and 880 °C ( $T_5$ ). Peak  $T_0$  corresponded to the reduction of Ru ions from a higher valence state to a lower valence state [55, 56]. Peaks  $T_1$  to  $T_4$  exhibited similar ionic valence state changes as observed in PSFN, while  $T_5$  corresponded to the reduction of low-valent Fe, Ni and Ru cations to FeNiRu metallic alloy. From the test results, the temperatures of  $T_1$  and  $T_2$  for PSFNrRu were significantly lower than that of PSFN, indicating that Ru doping promoted the reduction of Fe and Ni metal cations from a higher valence state to a lower valence state. However,  $T_5$  shifted to a higher temperature by approximately

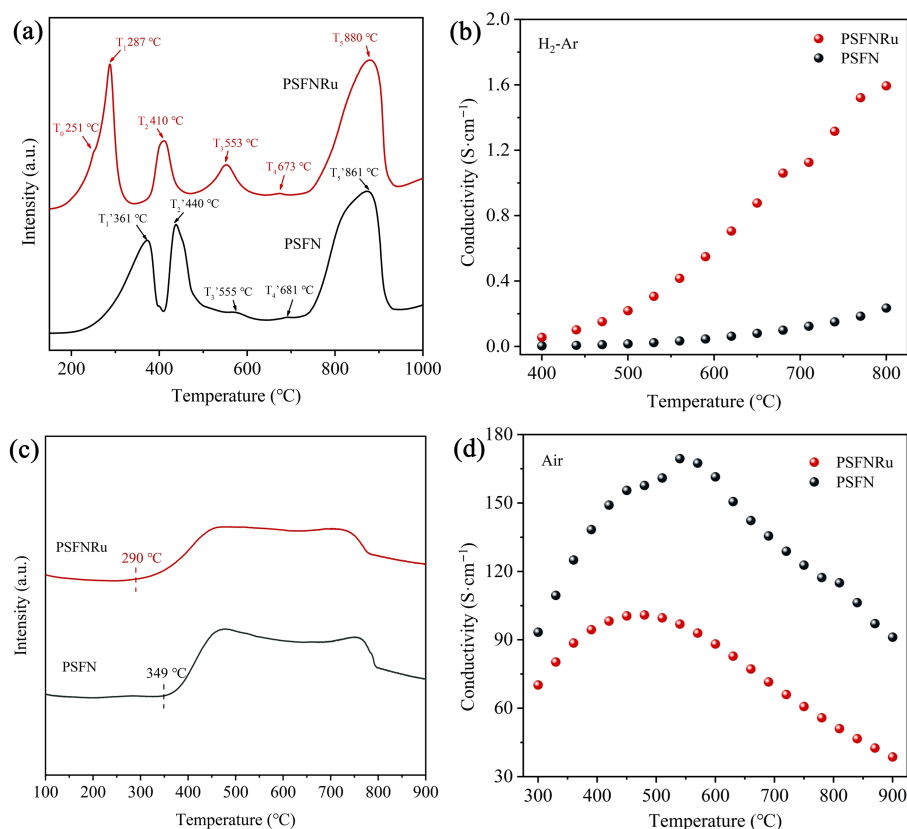


**Figure 3** The curves of PSFN and PSFNru for (a)  $\text{H}_2$ -TPR and (c)  $\text{O}_2$ -TPD. The electrical conductivity of PSFN and PSFNru in (b)  $\text{H}_2$ -Ar and (d) air.

20 °C, indicating an enhanced interaction between the *in-situ* exsolved ANPs and the perovskite matrix. The electrical conductivities of PSFN and PSFNru were evaluated under 10 vol.%  $\text{H}_2$ -Ar atmosphere. As demonstrated in Fig. 3(b), the electrical conductivity of PSFNru (0.056–1.593  $\text{S}\cdot\text{cm}^{-1}$ ) was superior to that of PSFN (0.005–0.235  $\text{S}\cdot\text{cm}^{-1}$ ) under 10 vol.%  $\text{H}_2$ -Ar atmosphere, indicating that PSFNru as an anode material had better electronic transfer and exchange capabilities than PSFN. The  $\text{O}_2$ -TPD curves, as illustrated in Fig. 3(c), reveal a reduction in the initial desorption temperature, decreasing from 349 °C in PSFN to 290 °C in PSFNru. The decrease in desorption temperature indicated that the PSFNru sample possesses enhanced surface oxygen exchange and oxygen ion migration capabilities [57], further demonstrating its potential as an excellent cathode material. From Fig. 3(d), the electrical conductivity of PSFNru under air atmosphere was lower than that of PSFN. This might be due to Ru doping promoted the reduction of  $\text{Fe}^{4+}$  to  $\text{Fe}^{3+}$ , leading to the formation of oxygen vacancies, which reduced the charge carrier concentration, thereby, resulting in decreased electrical conductivity [58]. Despite exhibiting lower electrical conductivity in air compared to PSFN, PSFNru still achieved a peak conductivity of 100  $\text{S}\cdot\text{cm}^{-1}$ , without negatively affecting the ORR process.

The electrochemical activity of PSFN and PSFNru towards ORR and HOR was evaluated through EIS analysis. Half-cells with a PSFN/PSFNru|SDC|PSFN/PSFNru structure were prepared for impedance testing. Figures 4(a) and 4(c) showed the Nyquist plots of PSFN and PSFNru in 10 vol.%  $\text{H}_2$ -Ar and air, respectively, at the temperatures range of 650 to 800 °C. To investigate the HOR activity of PSFN and PSFNru, impedance testing was conducted in a 10 vol.%  $\text{H}_2$ -Ar atmosphere. As illustrated in Fig. 4(a), PSFNru-based half-cell obtained lower area-specific resistance (ASR) values

than of PSFN-based half-cell at testing temperatures. For example, the ASR value of PSFNru-based half-cell at 800 °C was 0.027  $\Omega\cdot\text{cm}^2$ , 40% lower than that of PSFN-based half-cell (0.045  $\Omega\cdot\text{cm}^2$ ). The reason for the excellent HOR catalytic capability of PSFNru-based half-cell was further investigated using the DRT method. The DRT fitting results were depicted in Fig. 4(b). These peaks could be divided into three distinct segments based on the frequency range: low frequency (LF, < 10 Hz), intermediate frequency (IF, 10–10<sup>3</sup> Hz), and high frequency (HF, > 10<sup>3</sup> Hz) [59]. The  $\text{P}_1$  and  $\text{P}_2$  peaks were associated with gas adsorption/dissociation and surface exchange processes during electrode reaction procedures, while the  $\text{P}_3$  peak had a relationship with the charge transfer processes [16, 60]. It is evident that, in comparison to the PSFN half-cell, the  $\text{P}_1$  and  $\text{P}_2$  peak areas of the PSFNru half-cell were reduced. This might be due to the Ru doping facilitating the *in-situ* exsolution of more ANPs, creating additional active sites for the anode, thereby enhancing the adsorption, activation, and dissociation of  $\text{H}_2$ .

In air, PSFNru exhibited low ASR values of 0.090, 0.046, 0.026, and 0.016  $\Omega\cdot\text{cm}^2$  at 650, 700, 750, and 800 °C, respectively, lower than that of PSFN (0.104, 0.052, 0.030, and 0.020  $\Omega\cdot\text{cm}^2$ ). Lower ASR values indicated better ORR activity. To further analyze the electrochemical reaction processes, the DRT technique was employed to investigate the ORR kinetics. The spectra obtained from testing PSFN and PSFNru at 700 °C in an air atmosphere revealed four characteristic peaks (Fig. 4(d)). The four characteristic peaks corresponded to gas diffusion ( $\text{F}_1$ ), ion transfer or surface exchange within the cathode body ( $\text{F}_2$ ,  $\text{F}_3$ ), and ion transfer from the cathode to the electrolyte and charge transfer ( $\text{F}_4$ ) [61, 62]. Compared to PSFN, the doping of Ru caused remarkable reduction

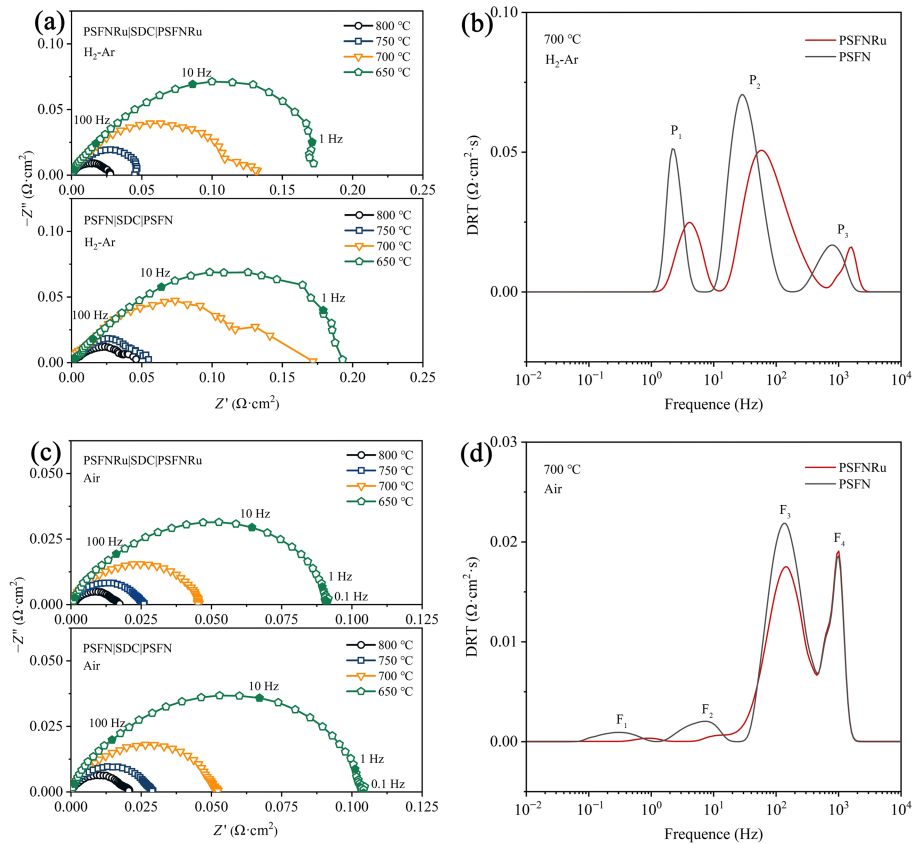


**Figure 4** EIS spectra of PSFN and PSFNru in (a) 10 vol.%  $\text{H}_2$ -Ar and (c) air. DRT results of EIS spectra measured at 700 °C in (b) 10 vol.%  $\text{H}_2$ -Ar and (d) air.

in the areas of the  $F_1$ ,  $F_2$  and  $F_3$  peaks, indicating that PSFNru exhibited improved performance in gas diffusion, oxygen surface exchange ability, and oxygen ion conduction.

It is widely recognized that achieving high catalytic activity for NDR is a crucial requirement for the anode in DA-SSOFCs. Consequently, the NDR catalytic performance of PSFN and PSFNru was tested, as illustrated in Fig. 5(a), to assess their efficiency. A noticeable enhancement in NDR catalytic activity was observed for PSFNru in comparison to PSFN, with the disparity in catalytic efficiency becoming increasingly evident, especially at temperatures below 700 °C. This was caused by the enhanced quantity and diminished particle size of the externally dispersed ANPs, which provided the perovskite with a greater number of active sites, thereby significantly improving the reaction kinetics. For example, the  $\text{NH}_3$  conversion rate of PSFNru at 600 °C was 74.5%, significantly higher than that of PSFN (52.58%). To evaluate the excellent performance of PSFNru as the electrode of DA-SSOFCs in actual work condition, symmetrical single cells with PSFNru as the electrode and SDC electrolyte were prepared and tested using  $\text{H}_2$  and  $\text{NH}_3$  as fuels. Prior to testing, considering economic factors and the potential impact of electrode calcination temperature on cell performance, a single cell with PSFN as the symmetric electrode was selected to evaluate the performance differences arising from various calcination temperatures. Calcination temperatures of 1100, 1000, and 900 °C were chosen, and the test results were presented in Fig. S5 in the ESM. When calcined at 1100 °C, the cell achieved a PPD of 458  $\text{mW}\cdot\text{cm}^{-2}$  at 800 °C using  $\text{NH}_3$  as the fuel, which was significantly higher than the PPDs of 385 and 254  $\text{mW}\cdot\text{cm}^{-2}$  obtained for electrodes calcined at 1000 and 900 °C, respectively. Therefore, 1100 °C was selected as

the calcination temperature for subsequent tests. To investigate the potential interfacial reactions between the PSFNru electrode and the SDC electrolyte, a 1:1 mass ratio mixture of PSFNru and SDC powders were prepared and calcined at 1100 °C in air for 2 h. As shown in Fig. S6 in the ESM, there was no other phases generation, indicating that no adverse reaction occurred between the PSFNru electrode and SDC electrolyte. Figures 5(b) and Fig. S7 in the ESM presented the typical  $I$ - $V$ - $P$  curves and EIS spectra of the single cell employing PSFNru as a symmetrical electrode. When using  $\text{NH}_3$  as fuel, the cell achieved PPDs of 547, 386, 264 and 166  $\text{mW}\cdot\text{cm}^{-2}$  at 800–650 °C, respectively, with corresponding polarization resistances ( $R_p$ ) of 0.025, 0.039, 0.068 and 0.123  $\Omega\cdot\text{cm}^2$ , demonstrating excellent electrochemical performance. As depicted in Fig. 5(c), and Figs. S8(a) and S8(d) in the ESM, the PSFNru-based single cell exhibited superior electrochemical performance when fueled with  $\text{H}_2$ . At 800, 750, 700 and 600 °C, the PPDs were 711, 555, 419 and 305  $\text{mW}\cdot\text{cm}^{-2}$ , respectively. The disparity in performance was likely ascribed to the increase Ohmic resistance ( $R_{\text{ohm}}$ ) and  $R_p$ . This was because the NDR was an endothermic process [63], leading to a localized temperature drop in the core reaction zone, thereby increasing  $R_{\text{ohm}}$ . The increased  $R_p$  was speculated to result from the fact that  $\text{NH}_3$  did not directly participate in SOFC power generation, and the additional decomposition step contributed to an increase in  $R_p$ .

Furthermore, as evidenced by the test results, the PSFNru-based symmetrical electrode single cell exhibited superior electrochemical performance relative to the PSFN cell under both  $\text{H}_2$  and  $\text{NH}_3$  fuel conditions at 800–650 °C (Fig 5(b) and Figs. S8(a)–S8(c) in the ESN). From Fig. 5(d) and Figs. S8(d)–S8(f) in the ESM, it was observed that the performance enhancement could be attributed to

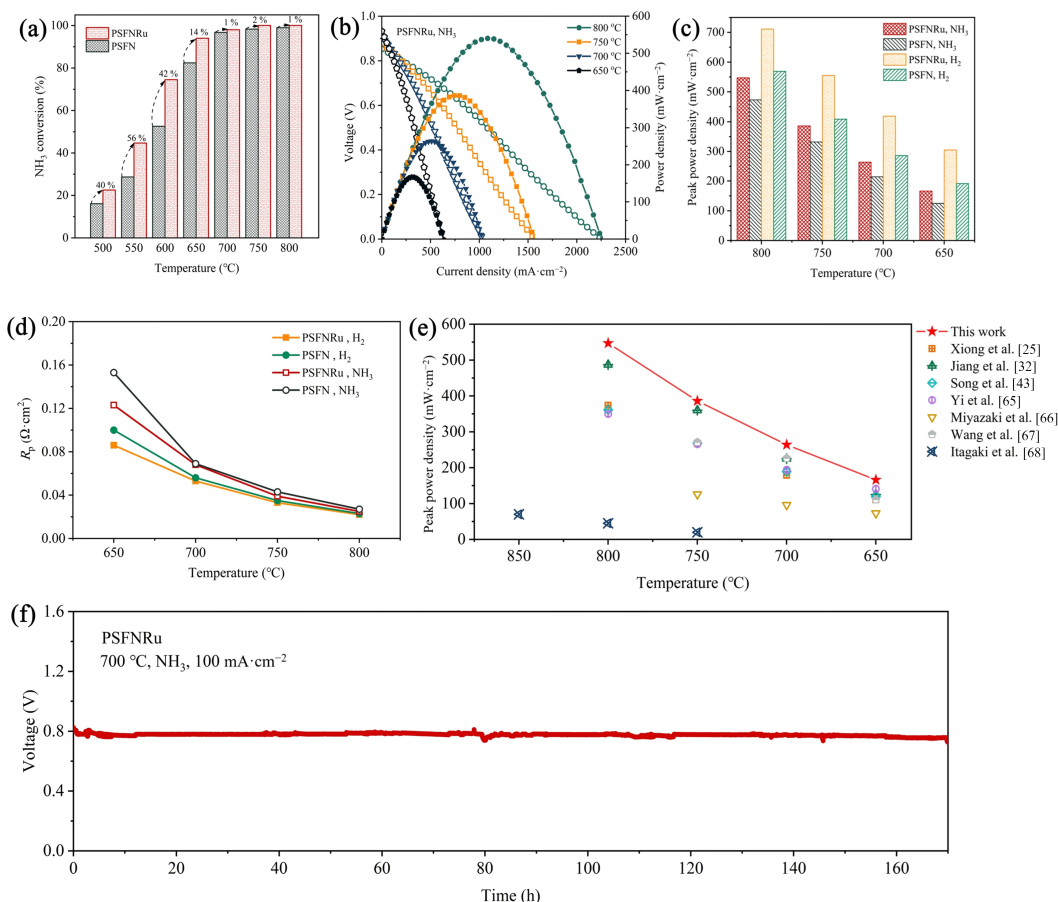


**Figure 5** (a) NDR catalytic activity tests of PSFN and PSFNru at 500–800 °C. (b) Current–voltage–power density ( $I$ – $V$ – $P$ ) curves of PSFNru operating with  $\text{NH}_3$ . (c) The PPDs of PSFN and PSFNru operating with  $\text{H}_2$ ,  $\text{NH}_3$  at 650–800 °C. (d)  $R_p$  of the cells with the PSFN and PSFNru operated at 650–800 °C in  $\text{H}_2$  and  $\text{NH}_3$ . (e) PPDs of PSFNru-based DA-SSOFC at 650–850 °C were compared with reported advanced DA-SOFCs. (f) Operational stability test of PSFNru-based DA-SSOFC.

the promoted  $\text{H}_2$  electro-oxidation, NDR and ORR facilitated by PSFNru, which resulted in a reduction in  $R_{\text{ohm}}$  and  $R_p$  [64]. As illustrated in Fig. 5(e) and Table S1 in the ESM, compared to advanced DA-SOFCs reported in the literature [25, 32, 43, 65–68], the PSFNru symmetrical electrode achieved superior electrochemical performance through a simple elemental doping strategy and the *in-situ* exsolution of ANPs from the anode, demonstrating strong competitiveness. The power output of this cell exhibited a significant advantage over many previously reported electrolyte-supported advanced DA-SOFCs and even surpassed some anode-supported DA-SOFCs.

Traditional nickel-based anodes experienced severe agglomeration in  $\text{NH}_3$  fuel, which significantly affects the prolonged operational stability of DA-SOFCs. Thus, the prolonged durability of the DA-SSOFC employed PSFNru as a symmetrical electrode was investigated. As described in Fig. 5(f), under a current density of  $100 \text{ mA}\cdot\text{cm}^{-2}$  at  $700 \text{ }^\circ\text{C}$ , the PSFNru symmetrical single cell demonstrated stable operation for 172 h in  $\text{NH}_3$  fuel, with a voltage degradation rate of  $0.00048 \text{ V}\cdot\text{h}^{-1}$ . As visualized in Figs. S9(a) and S9(b) in the ESM, the microstructure of the PSFNru single cell was examined using SEM after stability testing. No separation was observed between the electrode and electrolyte, and no significant particle aggregation was detected on the anode. This further confirmed the high durability of PSFNru as an electrode in DA-SSOFCs.

## 4 Conclusions

On the whole, we demonstrated that PSFNru exhibited excellent electrocatalytic activity and stability as a DA-SSOFC symmetrical electrode. The doping of Ru in the parent perovskite led to the *in-situ* exsolution of ANPs under a reducing atmosphere, which increased the active sites on the electrode. This was the reason for PSFNru's superior NDR and HOR performance. Analysis from O 1s XPS and DRT indicated that the surface of PSFNru had more oxygen vacancies and a stronger oxygen surface exchange capability. Consequently, the DA-SSOFC with the PSFNru [SDC] PSFNru structure exhibited outstanding PPD ( $547 \text{ mW}\cdot\text{cm}^{-2}$  at  $800 \text{ }^\circ\text{C}$ ) and good operational stability (voltage degradation rate of  $0.00048 \text{ V}\cdot\text{h}^{-1}$ ). This work reported an efficient and durable perovskite-based nanocomposite symmetrical electrode material, advancing the technological utilization of DA-SSOFCs.

**Electronic Supplementary Material:** Supplementary material (XRD patterns, SEM images, particle size distributions, XPS,  $I$ – $V$ – $P$  curves and EIS spectra, and PPD data comparison table) is available in the online version of this article at <https://doi.org/10.26599/NR.2025.94907402>.

## Data availability

All data needed to support the conclusions in the paper are presented in the manuscript and the ESM. Additional data related

to this paper may be requested from the corresponding author upon request.

## Acknowledgements

This work is granted by the National Natural Science Foundation of China (Nos. 22309067 and 22279057) and Financial Program of BJAST (No. 25CA002).

## Declaration of competing interest

All the contributing authors report no conflict of interests in this work.

## Author contribution statement

Z. X. L.: Date curation, investigation, and writing draft. S. S. J.: Date curation, manuscript review and editing. Z. H. X. and Y. N. Y.: Investigation. J. J. J.: Manuscript review and editing. W. W., H. G. S. and L. G.: Instrumentation. C. S.: Funding procurement, experimental design, manuscript review and editing.

## Use of AI statement

None.

## References

- Hu, Y. M.; Chao, T. T.; Dou, Y. H.; Xiong, Y. L.; Liu, X. W.; Wang, D. S. Isolated metal centers activate small molecule electrooxidation: Mechanisms and applications. *Adv. Mater.* **2025**, 2418504.
- Wang, M.; Su, C.; Zhu, Z. H.; Wang, H.; Ge, L. Composite cathodes for protonic ceramic fuel cells: Rationales and materials. *Compos. Part B Eng.* **2022**, *238*, 109881.
- Li, Y. X.; Li, Y.; Jiang, S. S.; Chen, Y. B.; Xu, J. H.; Qiu, H.; Su, C.; Ge, L. La-doped Sr<sub>4</sub>Fe<sub>4</sub>Co<sub>2</sub>O<sub>13-δ</sub> as a promising *in-situ* self-assembled composite cathode for protonic ceramic fuel cells. *Compos. Part B Eng.* **2024**, *280*, 111517.
- Li, Q. W.; Jiang, J. J.; Jiang, S. S.; Liu, D.; Xu, D. H.; Chen, Y. J.; Zhu, D. R.; Liu, X. W. Catalyst design for the electrochemical reduction of carbon dioxide: From copper nanoparticles to copper single atoms. *Microstructures* **2025**, *5*, 2025003.
- Li, Q.; Li, Q.; Wang, Z. W.; Zheng, X. B.; Cai, S. C.; Wu, J. B. Recent advances in hierarchical porous engineering of MOFs and their derived materials for catalytic and battery: Methods and application. *Small* **2024**, *20*, 2303473.
- Liu, Y.; Shao, Z. P.; Mori, T.; Jiang, S. P. Development of nickel based cermet anode materials in solid oxide fuel cells - Now and future. *Mater. Rep. Energy* **2021**, *1*, 100003.
- Belotti, A.; Liu, J. P.; Curcio, A.; Wang, J.; Wang, Z.; Quattrocchi, E.; Effat, M. B.; Ciucci, F. Introducing Ag in Ba<sub>0.9</sub>La<sub>0.1</sub>FeO<sub>3-δ</sub>: Combining cationic substitution with metal particle decoration. *Mater. Rep. Energy* **2021**, *1*, 100018.
- Qiu, H.; Liang, M. Z.; Zhao, J.; Liang, Z. X.; Jiang, S. S.; Shi, H. G.; Wang, W.; Wen, H. B.; Su, C. A-site cation deficient SrTa<sub>0.1</sub>Fe<sub>0.9</sub>O<sub>3-δ</sub> as a bi-functional cathode for both oxygen ion and proton-conducting solid oxide fuel cells. *Ceram. Int.* **2024**, *50*, 40500–40509.
- Tang, B.; Ji, Q. Q.; Zhang, X. L.; Shi, R. C.; Ma, J.; Zhuang, Z. C.; Sun, M.; Wang, H. J.; Liu, R. Q.; Liu, H. J.; Wang, C.; Guo, Z. Y.; Lu, L. L.; Jiang, P.; Wang, D. S.; Yan, W. S. Symmetry breaking of FeN<sub>4</sub> moiety via edge defects for acidic oxygen reduction reaction. *Angew. Chem.* **2025**, *64*, e202424135.
- Xu, S. H.; Qiu, H.; Jiang, S. S.; Jiang, J. J.; Wang, W.; Xu, X. M.; Kong, W.; Chivurugwi, T. D.; Proskurin, A.; Chen, D. F. et al. New strategy for boosting cathodic performance of low temperature solid oxide fuel cells via chlorine doping. *Nano Res.* **2024**, *17*, 8086–8094.
- Gao, J. T.; Liu, Y. Y.; Gao, Y.; Yuan, M. K.; Wang, Z.; Lü, Z.; Li, Q.; Wei, B. Cobalt-free fluorine doped Bi<sub>0.7</sub>Sr<sub>0.3</sub>FeO<sub>3-δ</sub> oxides for energetic cathodes of low-temperature solid oxide fuel cells. *Chem. Eng. J.* **2023**, *452*, 139584.
- Yao, C. G.; Liu, W. N.; Zhang, H. X.; Wang, H. C.; Zhang, W. C.; Lang, X. S.; Cai, K. D. High-entropy perovskite (Pr<sub>1/6</sub>Nd<sub>1/6</sub>Sm<sub>1/6</sub>Ba<sub>1/6</sub>Sr<sub>1/6</sub>)<sub>6/7</sub>(Mn<sub>1/6</sub>Co)<sub>6/7</sub>O<sub>3-δ</sub> as a highly active and CO<sub>2</sub> durable cathode for solid oxide fuel cells. *Appl. Catal. B: Environ. Energy* **2025**, *363*, 124789.
- Yao, C. G.; Xia, B. X.; Zhang, H. X.; Wang, H. C.; Zhang, W. W.; Guo, Q. H.; Jiang, Y. B.; Lang, X. S.; Cai, K. D. Fluoride-driven modulation of oxygen vacancies and surface stability in cobalt-based perovskite as a high-performance cathode for solid oxide fuel cells. *Chem. Eng. J.* **2025**, *505*, 159359.
- Yuan, M. K.; Gao, Y.; Liu, L. M.; Gao, J. T.; Wang, Z.; Li, Y.; Hao, H. R.; Hao, W. T.; Lou, X. T.; Lv, Z. et al. High entropy double perovskite cathodes with enhanced activity and operational stability for solid oxide fuel cells. *J. Eur. Ceram. Soc.* **2024**, *44*, 3267–3276.
- Yang, G. M.; Su, C.; Shi, H. G.; Zhu, Y. L.; Song, Y. F.; Zhou, W.; Shao, Z. P. Toward reducing the operation temperature of solid oxide fuel cells: Our past 15 years of efforts in cathode development. *Energy Fuels* **2020**, *34*, 15169–15194.
- Yan, J.; Chen, H. L.; Li, Y. W.; Li, S. D.; Shao, Z. P. Bifunctional electrocatalysts Pr<sub>0.5</sub>Sr<sub>0.5</sub>Cr<sub>0.1</sub>Fe<sub>0.9-x</sub>Ni<sub>x</sub>O<sub>3-δ</sub> (x = 0.1, 0.2) for the HOR and ORR of a symmetric solid oxide fuel cell. *J. Mater. Chem. A* **2023**, *11*, 21839–21845.
- Zamudio-García, J.; Porras-Vázquez, J. M.; Losilla, E. R.; Marrero-López, D. Enhancing the electrochemical performance in symmetrical solid oxide cells through nanoengineered redox-stable electrodes with exsolved nanoparticles. *ACS Appl. Mater. Interfaces* **2024**, *16*, 555–568.
- Zhang, T. Y.; Jiang, J. J.; Sun, W. M.; Gong, S. Y.; Liu, X. W.; Tian, Y.; Wang, D. S. Spatial configuration of Fe–Co dual-sites boosting catalytic intermediates coupling toward oxygen evolution reaction. *Proc. Natl. Acad. Sci. USA* **2024**, *121*, e2317247121.
- Li, Y.; Ru, X. N.; Yang, M.; Zheng, Y. H.; Yin, S.; Hong, C. J.; Peng, F. G.; Qu, M. H.; Xue, C. W.; Lu, J. X.; Fang, L.; Su, C.; Chen, D. F.; Xu, J. H.; Yan, C.; Li, Z. G.; Xu, X. X.; Shao, Z. P. Flexible silicon solar cells with high power-to-weight ratios. *Nature* **2024**, *626*, 105–110.
- Yang, J. R.; Zhu, C. X.; Wang, D. S. A simple organo-electrocatalysis system for the chlor-related industry. *Angew. Chem.* **2024**, *63*, e202406883.
- Huang, Q.; Jiang, S. S.; Wang, Y. J.; Jiang, J. J.; Chen, Y. B.; Xu, J. H.; Qiu, H.; Su, C.; Chen, D. F. Highly active and durable triple conducting composite air electrode for low-temperature protonic ceramic fuel cells. *Nano Res.* **2023**, *16*, 9280–9288.
- He, F.; Gao, Q. N.; Liu, Z. Q.; Yang, M. T.; Ran, R.; Yang, G. M.; Wang, W.; Zhou, W.; Shao, Z. P. A new Pd doped proton conducting perovskite oxide with multiple functionalities for efficient and stable power generation from ammonia at reduced temperatures. *Adv. Energy Mater.* **2021**, *11*, 2003916.
- He, F.; Hou, M. Y.; Du, Z. W.; Zhu, F.; Cao, X. Z.; Ding, Y.; Zhou, Y. C.; Liu, M. L.; Chen, Y. Self-construction of efficient interfaces ensures high-performance direct ammonia protonic ceramic fuel cells. *Adv. Mater.* **2023**, *35*, 2304957.
- Somacescu, S.; Cioatera, N.; Osiceanu, P.; Calderon-Moreno, J. M.; Ghica, C.; Neațu, F.; Florea, M. Bimodal mesoporous NiO/CeO<sub>2-δ</sub>/YSZ with enhanced carbon tolerance in catalytic partial oxidation of methane-potential IT-SOFCs anode. *Appl. Catal. B: Environ.* **2019**, *241*, 393–406.
- Xiong, X. D.; Yu, J.; Huang, X. J.; Zou, D.; Song, Y. F.; Xu, M. G.; Ran, R.; Wang, W.; Zhou, W.; Shao, Z. P. Slightly ruthenium doping

- enables better alloy nanoparticle exsolution of perovskite anode for high-performance direct-ammonia solid oxide fuel cells. *J. Mater. Sci. Technol.* **2022**, *125*, 51–58.
- [26] Zhang, H.; Zhou, Y.C.; Pei, K.; Pan, Y.X.; Xu, K.; Ding, Y.; Zhao, B.T.; Sasaki, K.; Choi, Y.; Chen, Y.; Liu, M. L. An efficient and durable anode for ammonia protonic ceramic fuel cells. *Energy Environ. Sci.* **2022**, *15*, 287–295.
- [27] Shi, H. G.; Tang, J. Y.; Yu, W. Q.; Tadé, M. O.; Shao, Z. P. Advances in power generation from ammonia via electrocatalytic oxidation in direct ammonia fuel cells. *Chem. Eng. J.* **2024**, *488*, 150896.
- [28] Li, Y.; Pillai, H. S.; Wang, T.; Hwang, S.; Zhao, Y.; Qiao, Z.; Mu, Q. M.; Karakalos, S.; Chen, M. J.; Yang, J.; Su, D.; Xin, H. L.; Yan, Y. S.; Wu, G. High-performance ammonia oxidation catalysts for anion-exchange membrane direct ammonia fuel cells. *Energy Environ. Sci.* **2021**, *14*, 1449–1460.
- [29] Xu, K.; Zhu, F.; Hou, M. Y.; Li, C. N.; Zhang, H.; Chen, Y. Activating and stabilizing the surface of anode for high-performing direct-ammonia solid oxide fuel cells. *Nano Res.* **2023**, *16*, 2454–2462.
- [30] Wang, Y.; Ma, F. Y.; Zhang, G. Q.; Zhang, J. W.; Zhao, H.; Dong, Y. M.; Wang, D. S. Precise synthesis of dual atom sites for electrocatalysis. *Nano Res.* **2024**, *17*, 9397–9427.
- [31] Hubert, M.; Laurencin, J.; Cloetens, P.; Morel, B.; Montinaro, D.; Lefebvre-Joud, F. Impact of Nickel agglomeration on Solid Oxide Cell operated in fuel cell and electrolysis modes. *J. Power Sources* **2018**, *397*, 240–251.
- [32] Jiang, H.; Liang, Z. X.; Qiu, H.; Yi, Y. N.; Jiang, S. S.; Xu, J. H.; Wang, W.; Su, C.; Yang, T. A high-performance and durable direct-ammonia symmetrical solid oxide fuel cell with nano  $\text{La}_{0.6}\text{Sr}_{0.4}\text{Fe}_{0.7}\text{Ni}_{0.2}\text{Mo}_{0.1}\text{O}_{3-\delta}$ -decorated doped ceria electrode. *Nanomaterials* **2024**, *14*, 673.
- [33] Li, P.; Yang, B.; Chen, J.; Li, B.; Ma, L. S.; Wang, M. J.; Sun, X. Z.; Tian, Y. F.; Chi, B. Enhanced electrocatalytic activity and stability of high performance symmetrical solid oxide fuel cells with praseodymium-doped  $\text{SrCo}_{0.2}\text{Fe}_{0.8}\text{O}_{3-\delta}$  electrodes. *J. Mater. Chem. A* **2024**, *12*, 31895–31901.
- [34] Zhou, J.; Wang, N.; Cui, J. J.; Wang, J. K.; Yang, J. M.; Zong, Z.; Zhang, Z. H.; Chen, Q. C.; Zheng, X. C.; Wu, K. Structural and electrochemical properties of B-site Ru-doped  $(\text{La}_{0.8}\text{Sr}_{0.2})_{0.9}\text{Sc}_{0.2}\text{Mn}_{0.8}\text{O}_{3-\delta}$  as symmetrical electrodes for reversible solid oxide cells. *J. Alloy. Compd.* **2019**, *792*, 1132–1140.
- [35] Wang, L. G.; Wu, J. B.; Wang, S. W.; Liu, H.; Wang, Y.; Wang, D. S. The reformation of catalyst: From a trial-and-error synthesis to rational design. *Nano Res.* **2024**, *17*, 3261–3301.
- [36] Qin, M. X.; Tan, T.; Li, K.; Wang, Z. M.; Yang, H. Y.; Liu, Z. J.; Zhou, M. Y.; Liu, T. K.; Yang, C. H.; Liu, M. *In-situ* exsolved FeRu alloy nanoparticles on Ruddlesden-Popper oxides for direct hydrocarbon fuel solid oxide fuel cells. *Int. J. Hydrogen Energy* **2020**, *45*, 21464–21472.
- [37] Song, Y.; Kim, H.; Jang, J. H.; Bai, W. J.; Ye, C. C.; Gu, J. M.; Bu, Y. F.  $\text{Pt}_3\text{Ni}$  alloy nanoparticle electro-catalysts with unique core-shell structure on oxygen-deficient layered perovskite for solid oxide cells. *Adv. Energy Mater.* **2023**, *13*, 2302384.
- [38] Kim, H.; Lim, C.; Gu, J. M.; Jeong, H. Y.; Han, J. W.; Jang, J. H.; Bu, Y. F. Insight on strain relaxation effect in perovskites for high-temperature hydrogen oxidation reaction. *Adv. Energy Mater.* **2024**, *14*, 2401307.
- [39] Mu, X. Q.; Liu, S. L.; Zhang, M. Y.; Zhuang, Z. C.; Chen, D.; Liao, Y. R.; Zhao, H. Y.; Mu, S. C.; Wang, D. S.; Dai, Z. H. Symmetry-broken Ru nanoparticles with parasitic Ru-Co dual-single atoms overcome the volmer step of alkaline hydrogen oxidation. *Angew. Chem. Int. Ed.* **2024**, *63*, e202319618.
- [40] Guan, S. Y.; Yuan, Z. L.; Zhao, S. Q.; Zhuang, Z. C.; Zhang, H. H.; Shen, R. F.; Fan, Y. P.; Li, B. J.; Wang, D. S.; Liu, B. Z. Efficient hydrogen generation from ammonia borane hydrolysis on a tandem ruthenium-platinum-titanium catalyst. *Angew. Chem.* **2024**, *63*, e202408193.
- [41] Gan, T.; Wang, D. S. Atomically dispersed materials: Ideal catalysts in atomic era. *Nano Res.* **2024**, *17*, 18–38.
- [42] Shen, J.; Tang, M. H.; Shi, Z. H.; Guan, S. Y.; Shi, Y. J.; Zhuang, Z. C.; Li, R. Z.; Yang, J. R.; He, D. P.; Liu, B. Z.; Dou, Y. H.; Wang, D. S. Efficient generation of negative hydrogen with bimetallic-ternary-structured catalysts for nitrobenzene hydrogenation. *Angew. Chem.* **2025**, e202423626.
- [43] Song, Y. F.; Li, H. D.; Xu, M. G.; Yang, G. M.; Wang, W.; Ran, R.; Zhou, W.; Shao, Z. P. Fuel Cells: Infiltrated NiCo alloy nanoparticle decorated perovskite oxide: a highly active, stable, and antisintering anode for direct-ammonia solid oxide fuel cells (Small 28/2020). *Small* **2020**, *16*, 2070154.
- [44] Quattrocchi, E.; Wan, T. H.; Belotti, A.; Kim, D.; Pepe, S.; Kalinin, S. V.; Ahmadi, M.; Ciucci, F. The deep-DRT: A deep neural network approach to deconvolve the distribution of relaxation times from multidimensional electrochemical impedance spectroscopy data. *Electrochim. Acta* **2021**, *392*, 139010.
- [45] Qin, M. X.; Xiao, Y.; Yang, H. Y.; Tan, T.; Wang, Z. M.; Fan, X. M.; Yang, C. H. Ru/Nb co-doped perovskite anode: Achieving good coking resistance in hydrocarbon fuels via core-shell nanocatalysts exsolution. *Appl. Catal. B: Environ.* **2021**, *299*, 120613.
- [46] Liang, M. Z.; Song, Y. F.; Xiong, B. C.; Liu, D. L.; Xue, D. X.; Shen, L. Y.; Shi, K. H.; Song, Y. X.; Li, J. W.; Niu, Q. *In situ* exsolved CoFeRu alloy decorated perovskite as an anode catalyst layer for high-performance direct-ammonia protonic ceramic fuel cells. *Adv. Funct. Mater.* **2024**, *34*, 2408756.
- [47] Du, Z. H.; Zhao, H. L.; Yi, S.; Xia, Q.; Gong, Y.; Zhang, Y.; Cheng, X.; Li, Y.; Gu, L.; Świerczek, K. High-performance anode material  $\text{Sr}_2\text{FeMo}_{0.65}\text{Ni}_{0.35}\text{O}_{6-\delta}$  with *in situ* exsolved nanoparticle catalyst. *ACS Nano* **2016**, *10*, 8660–8669.
- [48] Fu, Z. W.; Hu, J. T.; Hu, W. L.; Yang, S. Y.; Luo, Y. F. Quantitative analysis of  $\text{Ni}^{2+}/\text{Ni}^{3+}$  in  $\text{Li}[\text{Ni}_x\text{Mn}_y\text{Co}_z]\text{O}_2$  cathode materials: Non-linear least-squares fitting of XPS spectra. *Appl. Surf. Sci.* **2018**, *441*, 1048–1056.
- [49] Yao, Q.; Huang, B. L.; Zhang, N.; Sun, M. Z.; Shao, Q.; Huang, X. Q. Channel-rich RuCu nanosheets for pH-universal overall water splitting electrocatalysis. *Angew. Chem.* **2019**, *131*, 14121–14126.
- [50] Liang, M. Z.; Song, Y. F.; Liu, D. L.; Xu, L. W.; Xu, M. G.; Yang, G. M.; Wang, W.; Zhou, W.; Ran, R.; Shao, Z. P. Magnesium tuned triple conductivity and bifunctionality of  $\text{BaCo}_{0.4}\text{Fe}_{0.4}\text{Zr}_{0.1}\text{Y}_{0.1}\text{O}_{3-\delta}$  perovskite towards reversible protonic ceramic electrochemical cells. *Appl. Catal. B: Environ.* **2022**, *318*, 121868.
- [51] Liang, M. Z.; Zhu, Y. J.; Song, Y. F.; Guan, D. Q.; Luo, Z. X.; Yang, G. M.; Jiang, S. P.; Zhou, W.; Ran, R.; Shao, Z. P. A new durable surface nanoparticles-modified perovskite cathode for protonic ceramic fuel cells from selective cation exsolution under oxidizing atmosphere. *Adv. Mater.* **2022**, *34*, 2106379.
- [52] Xiong, J.; Zhong, H.; Li, J.; Zhang, X. L.; Shi, J. W.; Cai, W. W.; Qu, K. G.; Zhu, C. Z.; Yang, Z. H.; Beckman, S. P. et al. Engineering highly active oxygen sites in perovskite oxides for stable and efficient oxygen evolution. *Appl. Catal. B: Environ.* **2019**, *256*, 117817.
- [53] Liu, Z. Q.; Lin, Y. X.; Nie, H. Y.; Liu, D. L.; Li, Y. W.; Zhao, X. S.; Li, T.; Yang, G. M.; Sun, Y. F.; Zhu, Y. et al. Highly active nanocomposite air electrode with fast proton diffusion channels via Er doping-induced phase separation for reversible proton ceramic electrochemical cells. *Adv. Funct. Mater.* **2024**, *34*, 2311140.
- [54] Lv, H. L.; Zhao, H. Y.; Cao, T. C.; Qian, L.; Wang, Y. B.; Zhao, G. H. Efficient degradation of high concentration azo-dye wastewater by heterogeneous Fenton process with iron-based metal-organic framework. *J. Mol. Catal. A: Chem.* **2015**, *400*, 81–89.
- [55] Wang, X. Y.; Peng, X. B.; Ran, H. Y.; Lin, B. Y.; Ni, J.; Lin, J. X.; Jiang, L. L. Influence of Ru substitution on the properties of  $\text{LaCoO}_3$  catalysts for ammonia synthesis: XAFS and XPS studies. *Ind. Eng. Chem. Res.* **2018**, *57*, 17375–17383.

- [56] Haynes, D. J.; Berry, D. A.; Shekhawat, D.; Spivey, J. J. Catalytic partial oxidation of *n*-tetradecane using Rh and Sr substituted pyrochlores: Effects of sulfur. *Catal. Today* **2009**, *145*, 121–126.
- [57] Liang, M. Z.; He, F.; Zhou, C.; Chen, Y. B.; Ran, R.; Yang, G. M.; Zhou, W.; Shao, Z. P. Nickel-doped BaCo<sub>0.4</sub>Fe<sub>0.4</sub>Zr<sub>0.1</sub>Y<sub>0.1</sub>O<sub>3-δ</sub> as a new high-performance cathode for both oxygen-ion and proton conducting fuel cells. *Chem. Eng. J.* **2021**, *420*, 127717.
- [58] Tan, T.; Qin, M. X.; Li, K.; Zhou, M. Y.; Liu, T. K.; Yang, C. H.; Liu, M. *In-situ* exsolved NiFe alloy nanoparticles on Pr<sub>0.8</sub>Sr<sub>1.2</sub>(NiFe)O<sub>4-δ</sub> for direct hydrocarbon fuel solid oxide fuel cells. *Int. J. Hydrogen Energy* **2020**, *45*, 29407–29416.
- [59] Chen, X.; Yu, N.; Bello, I. T.; Guan, D. Q.; Li, Z.; Liu, T.; Liu, T.; Shao, Z. P.; Ni, M. Facile anion engineering: A pathway to realizing enhanced triple conductivity in oxygen electrodes for reversible protonic ceramic electrochemical cells. *Energy Storage Mater.* **2023**, *63*, 103056.
- [60] Yang, Y.; Chen, Z. P.; Li, M. F.; Rao, M. M.; Jin, F. J.; Ling, Y. H.; Feng, P. Z.; Wang, S. R. A highly efficient bismuth substitution induced A-site ordered layered perovskite electrode for symmetrical solid oxide fuel cells. *J. Mater. Chem. A* **2023**, *11*, 7995–8002.
- [61] Huang, J. Y.; Xie, Z. K.; Ai, N.; Wang, C. C.; Jiang, S. P.; Wang, X.; Shao, Y. Q.; Chen, K. F. A hybrid catalyst coating for a high-performance and chromium-resistive cathode of solid oxide fuel cells. *Chem. Eng. J.* **2022**, *431*, 134281.
- [62] Zhou, X.; Yang, C. H.; Yang, C. C.; Li, J.; Chi, B. Self-assembled cathode induced by polarization for high-performance solid oxide fuel cell. *J. Mater. Chem. A* **2023**, *11*, 1785–1792.
- [63] Lucentini, I.; Garcia, X.; Vendrell, X.; Llorca, J. Review of the decomposition of ammonia to generate hydrogen. *Ind. Eng. Chem. Res.* **2021**, *60*, 18560–18611.
- [64] Zhang, H.; Xu, K.; Xu, Y. S.; He, F.; Zhu, F.; Sasaki, K.; Choi, Y.; Chen, Y. *In situ* formed catalysts for active, durable, and thermally stable ammonia protonic ceramic fuel cells at 550 °C. *Energy Environ. Sci.* **2024**, *17*, 3433–3442.
- [65] Yi, Y. N.; Chen, J. M.; Xu, M. G.; Yang, G. M.; Ran, R.; Zhou, W.; Wang, W.; Shao, Z. P. Exsolved nanoparticles decorated double perovskites as high-performance anodes for direct-ammonia solid oxide fuel cells. *Catalysts* **2023**, *13*, 996.
- [66] Miyazaki, K.; Okanishi, T.; Muroyama, H.; Matsui, T.; Eguchi, K. Development of Ni-Ba(Zr,Y)O<sub>3</sub> cermet anodes for direct ammonia-fueled solid oxide fuel cells. *J. Power Sources* **2017**, *365*, 148–154.
- [67] Wang, Y. H.; Yang, J.; Wang, J. X.; Guan, W. B.; Chi, B.; Jia, L. C.; Chen, J. Y.; Muroyama, H.; Matsui, T.; Eguchi, K. Low-temperature ammonia decomposition catalysts for direct ammonia solid oxide fuel cells. *J. Electrochem. Soc.* **2020**, *167*, 064501.
- [68] Itagaki, Y.; Cui, J.; Ito, N.; Aono, H.; Yahiro, H. Electrophoretically deposited Ni-loaded (SmO<sub>1.5</sub>)<sub>0.2</sub>(CeO<sub>2</sub>)<sub>0.8</sub> anode for ammonia-fueled solid oxide fuel cell. *ECS Trans.* **2018**, *85*, 779–786.



This is an open access article under the terms of the Creative Commons Attribution 4.0 International License (CC BY 4.0, <https://creativecommons.org/licenses/by/4.0/>).

© The Author(s) 2025. Published by Tsinghua University Press.